Invasion of homogeneous and polyploid populations in nutrient-limiting environments

Gregory J. Kimmel[1], Mark Dane[2], Laura Heiser[2,1], Philipp M. Altrock[1] and Noemi Andor[1*]

[1]Department of Integrated Mathematical Oncology, Moffitt Cancer Center, Tampa, FL, USA [2]Department of Biomedical Engineering, OHSU Center for Spatial Systems Biomedicine, Knight Cancer Institute, Oregon Health & Sciences University, Portland, OR, USA

Financial support

This work was supported by the National Cancer Institute R00CA215256 awarded to NA. PMA acknowledges support through the National Cancer Institute, part of the National Institutes of Health (NIH), under grant number P30-CA076292. LH acknowledges support through NIH research grants 1U54CA209988, U54-HG008100, Jayne Koskinas Ted Giovanis Foundation for Health and Policy, and Breast Cancer Research Foundation.

Conflict of Interest

The authors declare no potential conflicts of interest.

Keywords

Evolutionary tradeoffs, Aneuploidy, Polyploidy, Breast cancer, Mathematical Modeling, Whole genome doubling, Partial differential equations, Traveling waves

[*]Noemi Andor; Moffitt Cancer Center, SRB 23224 B2 3011 Holly Drive, 33612 Tampa; noemi.andor@moffitt.org

Supplementary Information

Model derivation

We suppose that the energy flux is driven entirely via diffusion with coefficient Γ_E dependent on the type of media. The energy is consumed in proportion to the amount of cells present. For cell motility, we assume it is driven both by chemokinesis and chemotaxis. This leads to our general coupled system

$$\frac{\partial \tilde{E}}{\partial t} = \Gamma_E \nabla^2 \tilde{E} - \delta \tilde{E}(U+V), \tag{S1a}$$

$$\frac{\partial U}{\partial t} = \nabla \cdot \left(\Gamma \nabla U - \chi U \frac{\nabla \tilde{E}}{\Xi_U + \tilde{E}} \right) + \lambda \frac{\tilde{E}}{\Phi_U + \tilde{E}} U \left(1 - \frac{U+V}{K} \right), \tag{S1b}$$

$$\frac{\partial V}{\partial t} = \nabla \cdot \left(\Gamma \nabla V - \chi V \frac{\nabla \tilde{E}}{\Xi_V + \tilde{E}} \right) + \lambda \frac{\tilde{E}}{\Phi_V + \tilde{E}} V \left(1 - \frac{U+V}{K} \right). \tag{S1c}$$

The system (S1) is defined on a dish of radius R subject to no-flux boundary conditions. We assume the cells U, V are initially concentrated at the center with radius $\rho_0 \leq R$ and initial concentrations U_0, V_0. Further, we assume that the energy density is uniformly distributed on the plate with initial value E_0. All parameters except otherwise stated are independent of any of the state variables $(\tilde{E}, U, V)$. The energy is consumed at rate δ. Both cells can divide at the maximal rate λ, but are restricted by the energy density $\tilde{E}$. The cells can grow to a local maximal density given by K. This parameter is often cell line-dependent and is related to contact inhibition and cells being able to grow on top of each other.

Before proceeding, we rescale our variables $\tilde{E}, U, V$. Define $E = \tilde{E}/E_0, u = U/K, v = V/K$. In other words, we are looking at the change in energy relative to the initial amount and normalizing the cells by their local carrying capacity density. This leads to a natural redefinition of the energy sensitivity parameters $\xi_i = \Xi_i/E_0$ and $\phi_i = \Phi_i/E_0$.

Next, we rescale time in terms of the maximal growth rate $\tau = \lambda t$ and introduce a characteristic length by $L = \sqrt{\chi/\lambda}$. With this rescaling, we have our main (non-dimensional) equations

$$\frac{\partial E}{\partial \tau} = \gamma_E \nabla^2 E - aE(u+v), \tag{S2a}$$

$$\frac{\partial u}{\partial \tau} = \nabla \cdot \left(b \nabla u - u \frac{\nabla E}{\xi_U + E} \right) + \frac{E}{\phi_U + E} u(1-u-v), \tag{S2b}$$

$$\frac{\partial v}{\partial \tau} = \nabla \cdot \left(b \nabla v - v \frac{\nabla E}{\xi_V + E} \right) + \frac{E}{\phi_V + E} v(1-u-v), \tag{S2c}$$

where we have defined $\gamma_E = \Gamma_E/\chi,\ a = \delta K/\lambda,\ b = \Gamma/\chi$.

We made a few choices that warrant further explanation. First, we were mainly interested in the degree of infiltration that the heterogeneous population would make given a finite source of energy. If the source was infinite, the growth rate term would never decay, and the cells would eventually make their way across the entire dish (both in simulations and eventually in experiments through random motion, if permitted). This energy source term is also non-trivial. For example, we can use a periodic energy source term where $q = q_0 \sin(2\pi t/T)$, or we can use a constant source term $q = q_0$. Ultimately, any source term which does not decay to zero at long times will eventually have the cells occupying the entire dish. Since we are mostly interested in how far they can move given a finite amount of energy, we avoided adding this additional term at this time.

Second, the inclusion of a local carrying capacity is to prohibit overgrowth of too many cells on top of each other. Different cell lines are expected to have different K's and cells that don't have this restriction can be modeled by taking $K \to \infty$. This also avoids potential overflow, when the half-maximal energy parameters $\phi \ll 1$. Ultimately, energy-dependent growth in a finite resource environment is a natural mechanism that stops growth, but a local carrying capacity is also a natural parameter as we don't expect unbounded stacking of cells.

Third, additional compartments that model the tumor microenvironment (e.g. normal cells, matrix tissue) were purposely omitted. The model has the ability to incorporate this through increasing complexity in a modeling hierarchy by making the parameters related to growth and motion dependent on these additional compartments. For immobile structures such as matrix tissue, we could generalize parameters to be spatially-dependent. For additional cell types (e.g. normal cells), we can add compartments to the model with growth- and motion-related parameters that are specific to the corresponding cell type. In this regard, our model is flexible and amendable to further additions.

Infiltration

An important question in cancer dynamics is infiltration into and through tissue. The desire for cells to move is inherently tied to the availability of nutrients and space. To this end we define $\Psi(\tau) := [\rho(\tau) - \rho_0]/\rho_0$ where $\rho(0) = \rho_0$, the initial radius of cell seeding density. Ψ can be thought of as a non-dimensional measure of infiltration attained after time τ. This dimensionless measure has the added benefit of being scale-independent. An inherent difficulty with random cell motility and calculating infiltration is that the system always reaches the boundary in finite time. Instead we will define the maximum degree of infiltration to be given by the time needed for the total energy to be below a threshold $\varepsilon \ll 1$. For simulations, we took the 1-norm $\|E\|_1 < \varepsilon = 1e-4$.

In general, the maximum degree of infiltration is difficult to predict analytically, so we will only consider the single population case when obtaining our analytical estimates. We will also make use of the simplification that most energy-type molecules (e.g. glucose) have a diffusion coefficient that is very large, relative to cell movement. This allows us to write the reduced model:

$$\frac{dE}{d\tau} = -a \left(\frac{\rho}{R} \right)^2 E(u+v), \tag{S3a}$$

$$\frac{\partial u}{\partial \tau} = b \nabla^2 u + \frac{E}{\phi_u + E} u(1-u), \tag{S3b}$$

The additional term $(\rho/R)^2$ arises due to the fact that energy is

now assumed to be homogeneous in space. Hence, (S2a) can be integrated over space, but we must account for the fact that E is uniform and u is non-zero only if $r \leq \rho(\tau)$. Performing this integration leads to the modification in (S3a).

No chemotaxis infiltration estimate

Consider (S3a) - (S3b), we write the radially symmetric Laplacian explicitly and obtain

$$\frac{dE}{d\tau} = -a\left(\frac{\rho}{R}\right)^2 Eu, \tag{S4}$$

$$\frac{\partial u}{\partial \tau} = b\left(\frac{\partial^2 u}{\partial r^2} + \frac{n-1}{r}\frac{\partial u}{\partial r}\right) + \frac{E}{\phi + E}u(1-u), \tag{S5}$$

where n is the dimension (typically $n = 2, 3$, for circular or spherical growth, respectively). We now seek traveling wave-like solutions, where we assume that the wave speed is a slow function of r and τ. The solution obtained will verify that these assumptions are valid for our system. Our ansatz takes the form $u(r, \tau) = U(r - \eta\tau) = U(z)$. Note that in spatial equilibrium, $u = 1$ is stable and $u = 0$ is an unstable steady state. If the unstable state is what governs the wave speed, then the wave is said to be "pulled", otherwise it is "pushed". Based on numerical simulations, we assume that the state $u = 1$ is traveling across the domain and therefore set $u = 1$ in (S4):

$$\frac{dE}{d\tau} = -a\left(\frac{\rho}{R}\right)^2 E, \tag{S6}$$

$$0 = b\frac{\partial^2 U}{\partial z^2} + \left(\eta + \frac{b(n-1)}{r}\right)\frac{\partial U}{\partial z} + \frac{E}{\phi + E}U(1-U). \tag{S7}$$

Following a similar analysis conducted by Kaper et. al. [59], we define the new spatial variable $r = z + \eta t = \rho + \tilde{z}$. Treating ρ and η as slowly varying functions we can replace the above equation in terms of $\tilde{z}$,

$$\frac{dE}{d\tau} = -a\left(\frac{\rho}{R}\right)^2 E, \tag{S8}$$

$$0 = b\frac{\partial^2 U}{\partial \tilde{z}^2} + \left(\eta + \frac{b(n-1)}{\rho + \tilde{z}}\right)\frac{\partial U}{\partial \tilde{z}} + \frac{E}{\phi + E}U(1-U). \tag{S9}$$

Treating ρ as a large constant gives the effective speed:

$$\tilde{\eta} = \eta + \frac{b(n-1)}{\rho}. \tag{S10}$$

We identify $\eta = d\rho/d\tau$ (the speed of the moving front) and so we have the evolution of the front given by the following coupled system:

$$\frac{dE}{d\tau} = -a\left(\frac{\rho}{R}\right)^2 E, \tag{S11}$$

$$\frac{d\rho}{d\tau} = 2\sqrt{\frac{bE}{\phi + E}} - \frac{b(n-1)}{\rho}. \tag{S12}$$

We see that our assumptions on the behavior of the traveling wave are verified. Since ρ is assumed much larger than 0 and $\rho/R \ll 1$, E is a slowly varying function of time and ρ is a slowly varying function of time and its size.

Estimating the degree of infiltration from equilibration

An interesting alternative to tracking the wave over time is to assume it travels as a wave, but only record the density after the system has reached uniformity. This is possible if the death rate (which has been neglected) is much smaller than the time it would take the cells to spread uniformly. If this is the case, we can bound the degree of infiltration from only knowing the uniform value at the end of the experiment. To see this, note that at the end of the wave, with energy now 0, the total number of cells u_T should remain fixed and so:

$$u_T = 2\pi\int_0^{\rho(T)} ur\, dr = 2\pi\rho(T)^2\int_0^1 u(\rho s)s\, ds. \tag{S13}$$

The uniform value $\bar{u}$ at confluence leads to:

$$u_T = 2\pi\bar{u}\int_0^R r\, dr = \pi\bar{u}R^2. \tag{S14}$$

Equating these gives an equation for the unknown $\rho(T)$:

$$[\rho(T)]^2 = \frac{\bar{u}R^2}{2\int_0^1 u(\rho s)s\, ds}. \tag{S15}$$

Note that $s \in [0, 1]$ is a measure of distance in terms of the location of the front. Let Λ be the width of the transition zone from $u = 1$ to $u = 0$, then we may partition the integral noting that $s < \Lambda$ implies that $u \approx 1$

$$\int_0^1 us\, ds = \int_0^\Lambda us\, ds + \int_\Lambda^1 us\, ds \approx \frac{\Lambda^2}{2} + \int_\Lambda^1 us\, ds. \tag{S16}$$

We now exploit the fact that $\langle u\rangle = 1/2$ in a symmetric integral about the midpoint of the transition zone [45]. Combining and simplifying gives the approximation for: $\rho(T)$

$$\rho(T) = R\sqrt{\frac{2\bar{u}}{1 + \Lambda^2}}. \tag{S17}$$

The infiltration is given by:

$$\Psi = \frac{R}{\rho_0}\sqrt{\frac{2\bar{u}}{1 + \Lambda^2}} - 1. \tag{S18}$$

Since we assume that the transition width is unknown, we can bound Ψ by considering $\Lambda = 0, 1$.

Model calibration using spatial growth patterns

Coordinates of all spots within a well were calculated based on Supplementary Fig. 1A. We calculated what percentage of the total cells seeded per well (2×10^5) fall within a spot. This was used to obtain the distribution of initial cell counts per spot (Supplementary Fig. 1B). To calculate the confluence of each spot at the time of

seeding, we assumed an average cell diameter of 26.77 μm and a spot diameter of 350 μm (Supplementary Fig. 1C).

Cells detected within each spot three days post-seeding were assigned to bins within a grid $\tilde{G} \in R^{20,20}$, whereby each entry of $\tilde{G}$ is associated with its corresponding xy-coordinates $O \in R^{20,20,2}$. The number of cells within each bin was averaged across all replicates of a given ECM, p. Let $c := max_{p,i,j}(\tilde{G}_{i,j}(p))$ be the number of cells per bin at 100% confluence. For all p, $\tilde{G}(p)$ was divided by c to obtain the $G(p)$ – the spatial distribution of confluence for p. For all entries of G, we calculated the euclidean distance, $D_{i,j}$, of its coordinates $O_{i,j}$ to the origin $(0,0)$ of the MEMA spot. For all bins $B_t := \{i,j | t-e \leq D_{i,j} \leq t+e\}$ within distance t to the origin, we then calculated the average confluence associated with that distance as:

$$\frac{1}{|B_t|} * \sum_{i,j \in B_t} G_{i,i} \tag{S19}$$

This was then compared to the confluence obtained from the simulations (Table 1) using the Wasserstein metric. 2.29% simulations fell within the bottom 0.05% quantile of Wasserstein distances and were considered representative for cellular growth on at least one ECM.

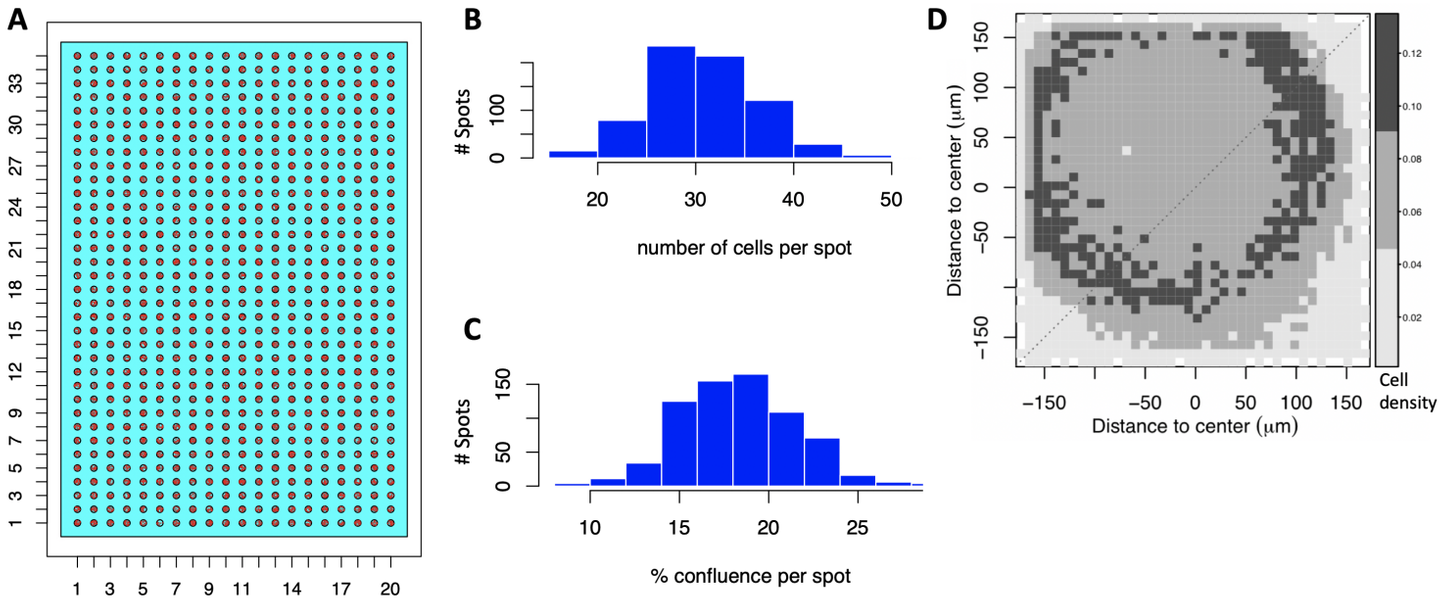

Supplementary Figure 1. MEMA array platform design. (A-C) Parameters inferred at the beginning of the MEMA assay. (A) Number of spots per row and column of a single well: 35×20; Diameter of a single spot: 350 μm; Horizontal and vertical distances between centers of two adjacent spots: 900 μm. Each spot image has 1600 x 1600 pixels, whereby 1 pixel = 321 nm. (B) Expected number of cells overlapping with a spot was calculated from parameters in (A), assuming 2×10^5 cells were distributed uniformly throughout the entire well [11, 60]. (C) Expected confluence per spot calculated from (B), assuming an average cell diameter of 26.77 μm. (D) Density distribution of spatial growth patterns is shown in aggregate across all spots in (A). Cell densities were measured at the end of the MEMA assay, after exposing HCC1954 cells to HGF for three days.

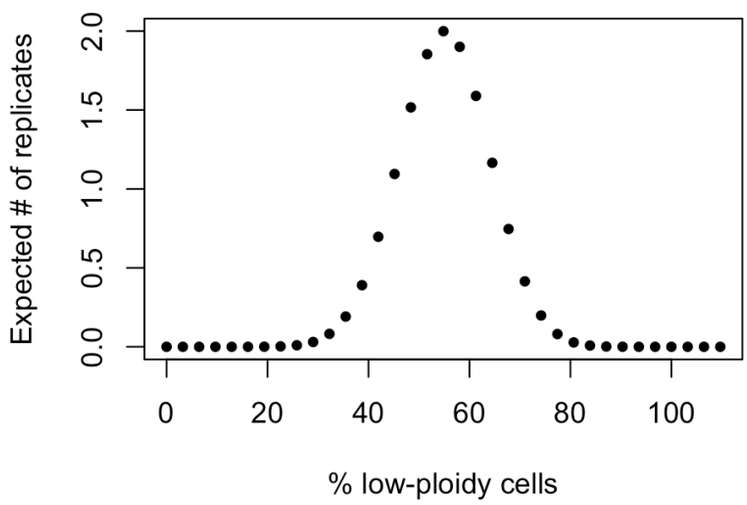

Supplementary Figure 2. Hypothetical example of the influence of population heterogeneity on reproducibility across MEP replicates. Probability of sampling given % low-ploidy cells when drawing 31 cells from a polyploid population (x-axis). Maximum probability shows true hypothetical incidence of low-ploidy cells (55% of the population). Probability was multiplied by the number of replicates (14) to obtain the values along the y-axis.

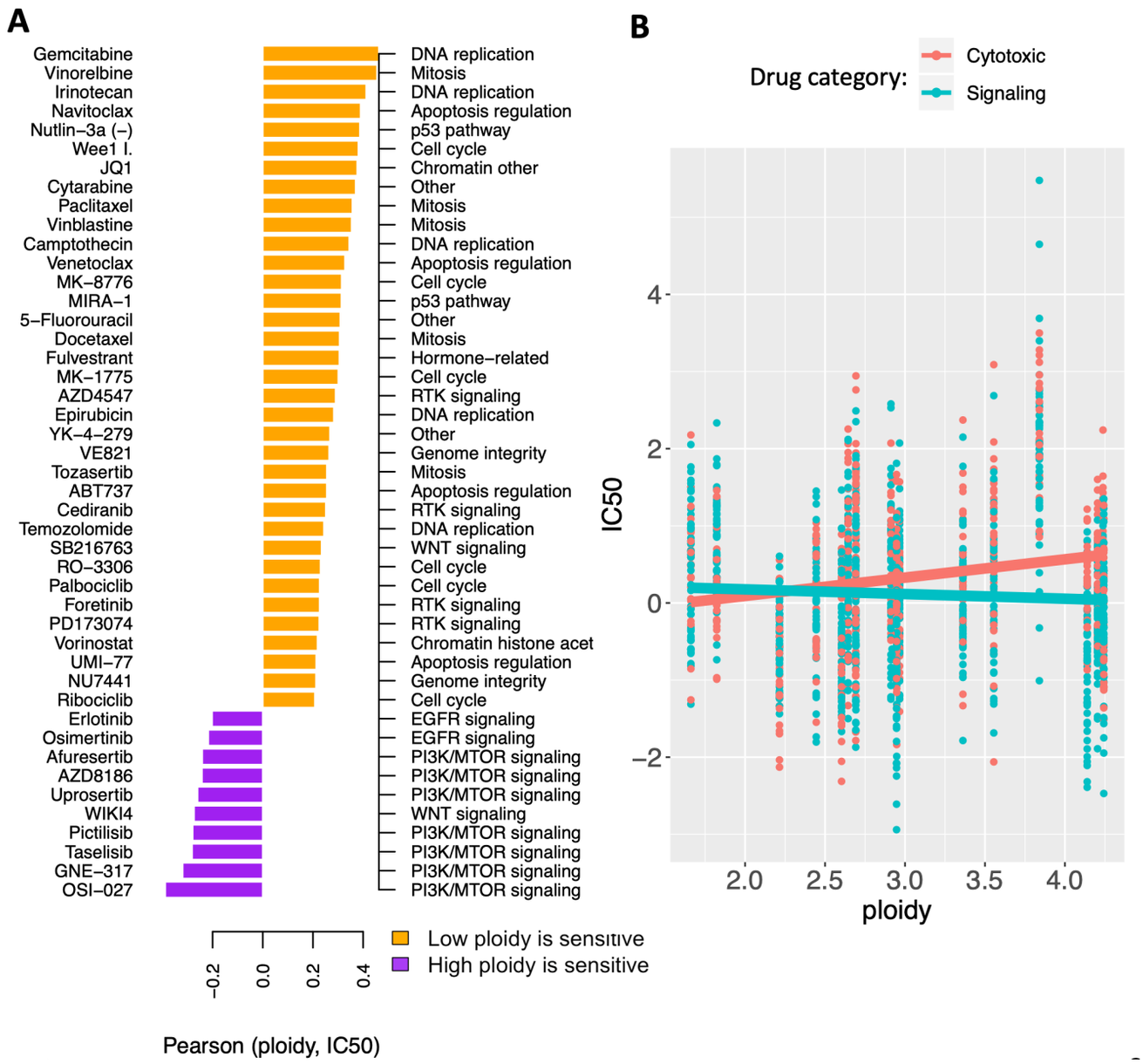

Supplementary Figure 3. Validation of ploidy as biomarker of drug sensitivity across breast cancer cell lines in an independent dataset. (A) High-ploidy breast cancer cell lines are resistant to cytotoxic drugs, but tend to be more sensitive to inhibitors of mTOR, EGFR and WNT signaling pathways. In a multivariate regression model of drug sensitivities molecular subtype alone (Fig. 1B), could explain 11% of the variability in IC50 values across cell lines (adjusted R-square = 0.109; $p < 1e\text{-}5$). Including ploidy into the model did minimally improve its predictive accuracy (adjusted R-square = 0.116; $p < 1e\text{-}5$). (B) However, an interaction term between ploidy and drug category increased accuracy to explain 14% of variability in drug sensitivity across cell lines (adjusted R-square = 0.142; $p < 1e\text{-}5$).

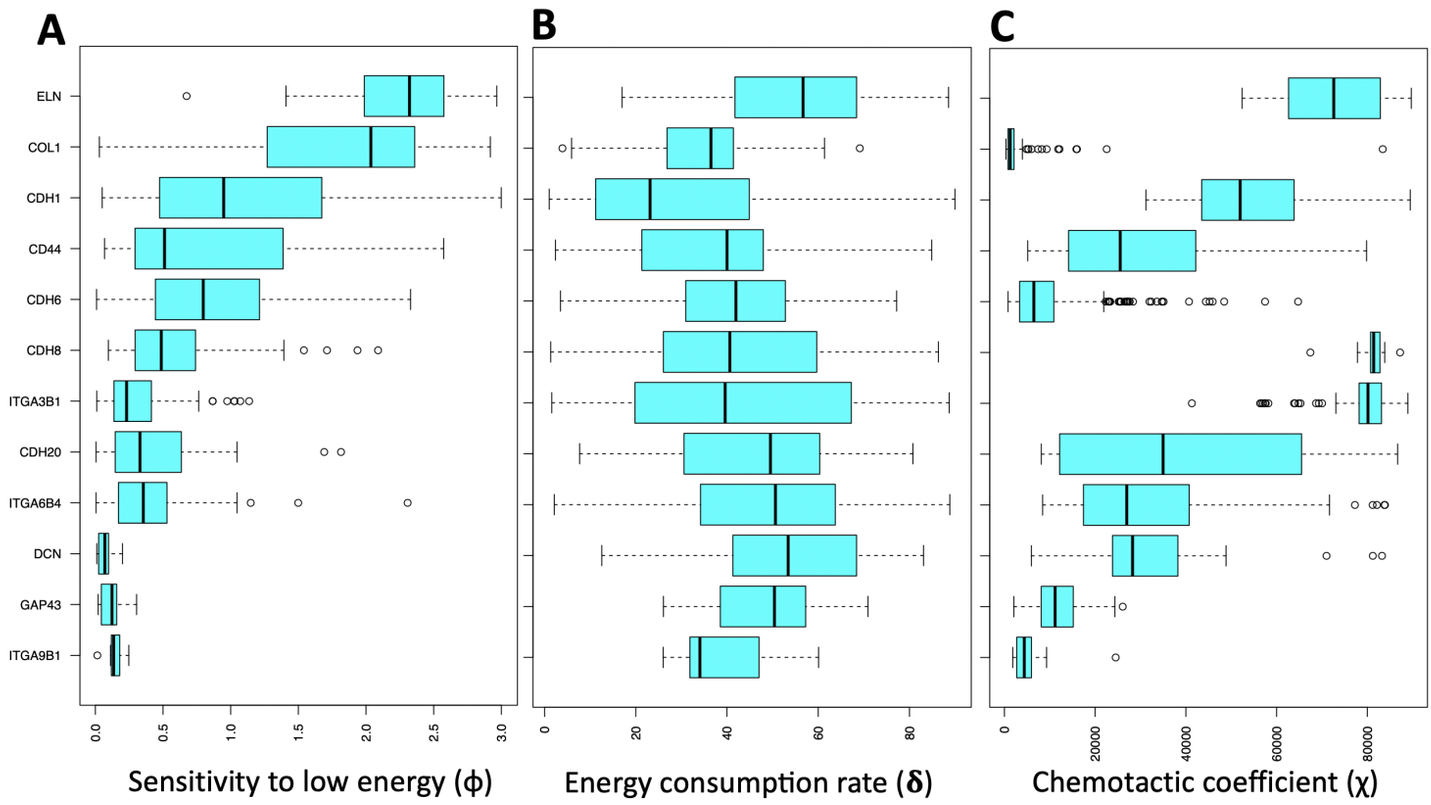

Supplementary Figure 4. Posterior parameter distributions per ECM. Best parameter fits for sensitivity to low energy (A), energy consumption rates (B) and chemotactic/haptotactic coefficients (C), stratified by the ECM they best explain.

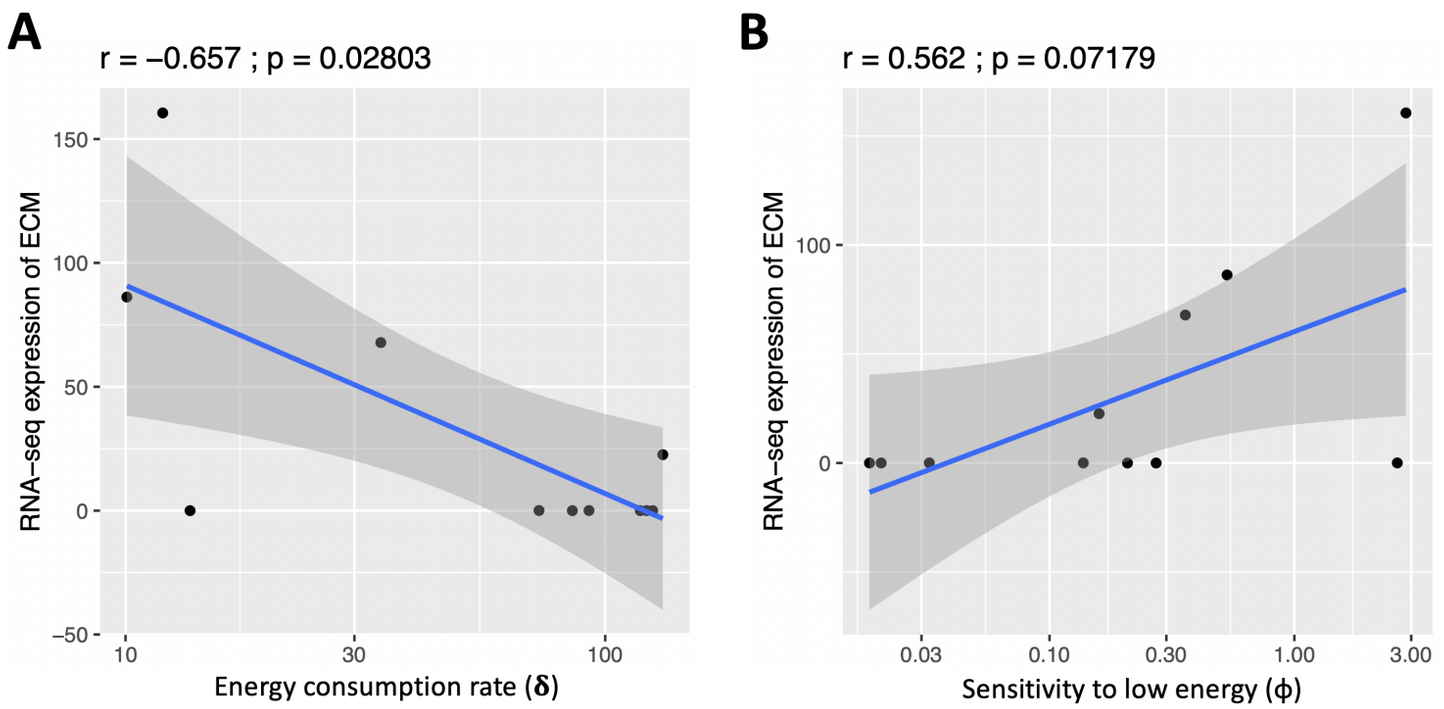

Supplementary Figure 5. Correlation between inferred model parameters and RNA-seq derived signatures. Model parameters a (energy consumption rate; A) and ϕ (sensitivity to low energy; B) vary across ECMs (x-axis), and this variability correlates with the expression of the corresponding ECM (y-axis). RNA-seq derived signatures were not used in any way to infer any model parameter.

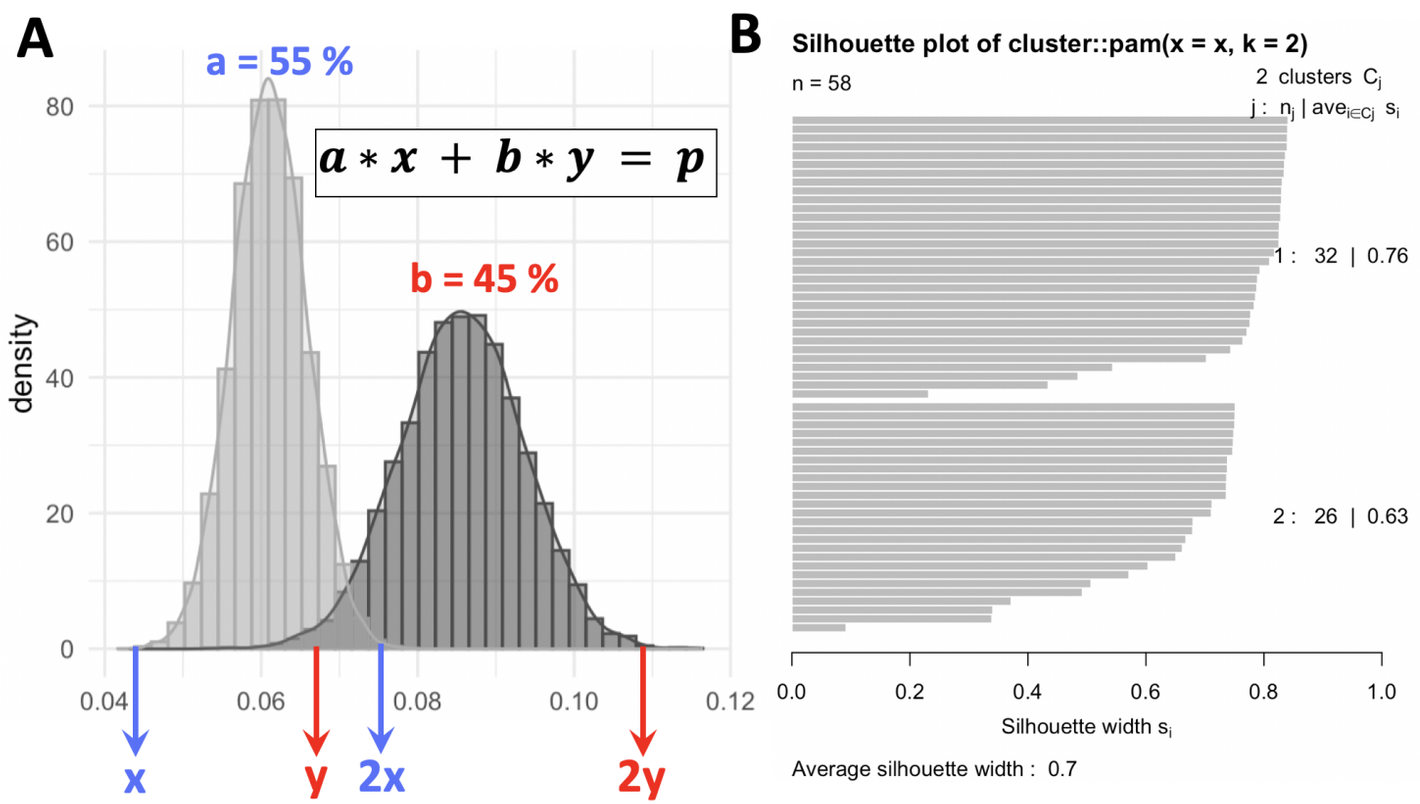

Supplementary Figure 6. Estimating the ploidies of co-existing clones in the HCC1954 cell line. (A) The bimodal distribution of DAPI content (x-axis) across EdU+ HCC1954 cells (y-axis) was used to infer the DNA contents of two clones thought to co-exist in the cell line (here denoted x and y respectively). The distribution informs the location of y as a function of x and the relative proportions of the two populations can also be read from the bimodal distributions of their S-phase cells. P denotes the population-average ploidy of the HCC1954 cell line (4.2). Solving for x yields ploidies 3.17 and 5.47 for the low and high-ploidy clone respectively. (B) Silhouette coefficient of each cell's assignment to one of the two clusters in (A). 18.9% of assignments (11 out of 58 cells) are ambiguous (silhouette coefficient < 0.6).

Parameter	Pearson coefficient	p-value
Metabolism of vitamins and cofactors	0.661	0.001
Metabolism of water-soluble vitamins and cofactors	0.597	0.005
Cytochrome P450 - arranged by substrate type	0.564	0.010
Hyaluronan metabolism	0.560	0.010
Hyaluronan uptake and degradation	0.560	0.010
Glycerophospholipid biosynthesis	0.556	0.011
O-linked glycosylation of mucins	0.553	0.011
Synthesis of PC	0.546	0.013
Termination of O-glycan biosynthesis	0.529	0.017
Abacavir transport and metabolism	0.520	0.019
Advanced glycosylation endproduct receptor signaling	0.513	0.021
Purine catabolism	0.513	0.021
EPH-ephrin mediated repulsion of cells	0.510	0.022
The canonical retinoid cycle in rods (twilight vision)	0.506	0.023
Keratinization	0.505	0.023
RA biosynthesis pathway	0.501	0.024
Dectin-2 family	0.501	0.025
POU5F1 (OCT4), SOX2, NANOG activate genes related to proliferation	0.490	0.028
Biological oxidations	0.486	0.030
GPVI-mediated activation cascade	0.472	0.036
Attenuation phase	0.470	0.037
Lipoprotein metabolism	0.468	0.037
CD28 dependent PI3K/Akt signaling	0.466	0.038
Activation of SMO	-0.464	0.040
Protein-protein interactions at synapses	-0.446	0.049
Ephrin signaling	0.445	0.049
CD28 co-stimulation	0.444	0.050

Supplementary Table 1. REACTOME pathways correlated to ploidy across 20 breast cancer cell lines from CCLE.

Name	Pathway	Drug Category
Doxorubicin	Cytotoxic	Cytotoxic
Gemcitabine	Cytotoxic	Cytotoxic
Paclitaxel	Cytotoxic	Cytotoxic
Irinotecan	DNA replication	Cytotoxic
Ixabepilone	Microtubuli	Cytotoxic
Docetaxel	Cytotoxic	Cytotoxic
Ms275	Cytotoxic	Cytotoxic
CPT-11	Cytotoxic	Cytotoxic
Taxol	Mitosis	Cytotoxic
Topotecan	DNA replication	Cytotoxic
(Z)-4-Hydroxytamoxifen	Cytotoxic	Cytotoxic
Trichostatin A	HDAC Inhibitor	Cytotoxic
Vorinostat	Cytotoxic	Cytotoxic
Geldanamycin	Cytotoxic	Cytotoxic
Oxaliplatin	DNA replication	Cytotoxic
Vinorelbine	Mitosis	Cytotoxic
Cisplatin	DNA replication	Cytotoxic
Pemetrexed	Replication	Cytotoxic
Bortezomib	Protein stability and degradation	Cytotoxic
Carboplatin	DNA	Cytotoxic
17-AAG	Cytotoxic	Cytotoxic
Nutlin 3a	MDM2 inhibitor, Apoptosis	Cytotoxic
CGC-11047	DNA replication	Cytotoxic
5-FU	Other	Cytotoxic
Imatinib	Apoptosis	Cytotoxic
Crizotinib	ALK/HGFR Inhibitor	Signaling
PS-1145	IKB kinase	Signaling
Rapamycin	Signaling	Signaling
Omipalisib	Signaling	Signaling
AG1478	Signaling	Signaling
PD184352	MEK1/2 inhibitor	Signaling
Sirolimus	PI3K/MTOR signaling	Signaling
Cetuximab	EGFR	Signaling
Gefitinib	EGFR signaling	Signaling
Pd0325901	MEK Inhibitor	Signaling
Trametinib	ERK MAPK signaling	Signaling
AG1024	MAPK/ERK2 signaling	Signaling
Lapatinib	HER1/EGFR/ERBB1 Inhibitor	Signaling
Erlotinib	EGFR signaling	Signaling

Supplementary Table 2. Drug classification.

Parameter	*Dimensional symbol*	Value	Units	*Dimensionless symbol*	Range	Identity
Maximal growth rate	λ	0.564	day^{-1}			
Radius of the dish	$\check{R}$	1750	µm	R	[4, 93]	
Energy consumption rate	δ	57 ‡	$cells^{-1}\ day^{-1}$	a	[2, 160]	$\delta = \lambda * a$
Energy diffusion	Γ_E	9500 ‡	$\mu m^2\ day^{-1}$	η	[0.01, 968]	$\Gamma_E = \chi * \eta$
Simulation time	T	3	days	τ	1.69	$T = \tau / \lambda$
Chemotactic coefficient	χ	5500 ‡	$\mu m^2\ day^{-1}$			$\chi = \lambda * L^2$
Characteristic length				L	[19, 399]	$L = \check{R} / R$

Supplementary Table 3. Conversion between dimensional and non-dimensional model parameters. Prior distributions of dimensionless parameters were drawn from the indicated ranges while ensuring uniform priors of dimensional parameters. The spatial growth patterns resulting from these prior distributions were compared to the MEMA data to obtain the maximum posterior estimates for dimensional parameters shown here.

References

1. Spiteri I, Caravagna G, Cresswell GD, Vatsiou A, Nichol D, Acar A, et al. Evolutionary dynamics of residual disease in human glioblastoma. Annals of Oncology: Official Journal of the European Society for Medical Oncology. 2019;30(3):456–463.

2. Brastianos PK, Carter SL, Santagata S, Cahill DP, Taylor-Weiner A, Jones RT, et al. Genomic Characterization of Brain Metastases Reveals Branched Evolution and Potential Therapeutic Targets. Cancer Discovery. 2015 Nov;5(11):1164–1177. 00040.

3. Angelova M, Mlecnik B, Vasaturo A, Bindea G, Fredriksen T, Lafontaine L, et al. Evolution of Metastases in Space and Time under Immune Selection. Cell. 2018 Oct;175(3):751–765.e16. Available from: http://www.sciencedirect.com/science/article/pii/S0092867418312303.

4. Hannibal RL, Chuong EB, Rivera-Mulia JC, Gilbert DM, Valouev A, Baker JC. Copy number variation is a fundamental aspect of the placental genome. PLoS genetics. 2014 May;10(5):e1004290.

5. Dewhurst SM, McGranahan N, Burrell RA, Rowan AJ, Grönroos E, Endesfelder D, et al. Tolerance of whole-genome doubling propagates chromosomal instability and accelerates cancer genome evolution. Cancer Discovery. 2014 Feb;4(2):175–185. 00068.

6. Bielski CM, Zehir A, Penson AV, Donoghue MTA, Chatila W, Armenia J, et al. Genome doubling shapes the evolution and prognosis of advanced cancers. Nature genetics. 2018 Aug;50(8):1189–1195. Available from: https://www.ncbi.nlm.nih.gov/pmc/articles/PMC6072608/.

7. Amend SR, Torga G, Lin KC, Kostecka LG, Marzo Ad, Austin RH, et al. Polyploid giant cancer cells: Unrecognized actuators of tumorigenesis, metastasis, and resistance. The Prostate. 2019;79(13):1489–1497. _eprint: https://onlinelibrary.wiley.com/doi/pdf/10.1002/pros.23877. Available from: https://onlinelibrary.wiley.com/doi/abs/10.1002/pros.23877.

8. Pienta KJ, Hammarlund EU, Axelrod R, Brown JS, Amend SR. Poly-aneuploid cancer cells promote evolvability, generating lethal cancer. Evolutionary Applications;n/a(n/a). _eprint: https://onlinelibrary.wiley.com/doi/pdf/10.1111/eva.12929. Available from: https://onlinelibrary.wiley.com/doi/abs/10.1111/eva.12929.

9. Zhang S, Mercado-Uribe I, Xing Z, Sun B, Kuang J, Liu J. Generation of cancer stem-like cells through the formation of polyploid giant cancer cells. Oncogene. 2014 Jan;33(1):116–128.

10. López S, Lim EL, Horswell S, Haase K, Huebner A, Dietzen M, et al. Interplay between whole-genome doubling and the accumulation of deleterious alterations in cancer evolution. Nature Genetics. 2020 Mar;52(3):283–293.

11. Watson SS, Dane M, Chin K, Tatarova Z, Liu M, Liby T, et al. Microenvironment-Mediated Mechanisms of Resistance to HER2 Inhibitors Differ between HER2+ Breast Cancer Subtypes. Cell systems. 2018 Mar;6(3):329–342.e6. Available from: https://www.ncbi.nlm.nih.gov/pmc/articles/PMC5927625/.

12. Keenan AB, Jenkins SL, Jagodnik KM, Koplev S, He E, Torre D, et al. The Library of Integrated Network-Based Cellular Signatures NIH Program: System-Level Cataloging of Human Cells Response to Perturbations. Cell Systems. 2018;6(1):13–24.

13. Pirkmajer S, Chibalin AV. Serum starvation: caveat emptor. American Journal of Physiology-Cell Physiology. 2011 May;301(2):C272–C279. Available from: https://www.physiology.org/doi/full/10.1152/ajpcell.00091.2011.

14. Growth of human diploid cells (strain MRC-5) in defined medium; replacement of serum by a fraction of serum ultrafiltrate. - PubMed - NCBI;. Available from: https://www.ncbi.nlm.nih.gov/pubmed/422676.

15. Bartholomew JC, Yokota H, Ross P. Effect of serum on the growth of balb 3T3 A31 mouse fibroblasts and an SV40-transformed derivative. Journal of Cellular Physiology. 1976 Jul;88(3):277–286. Available from: https://onlinelibrary.wiley.com/doi/10.1002/jcp.1040880303.

16. Cai W, Rook SL, Jiang ZY, Takahara N, Aiello LP. Mechanisms of hepatocyte growth factor-induced retinal endothelial cell migration and growth. Investigative Ophthalmology & Visual Science. 2000 Jun;41(7):1885–1893.

17. Hatzikirou H, Basanta D, Simon M, Schaller K, Deutsch A. 'Go or grow': the key to the emergence of invasion in tumour progression? Mathematical medicine and biology: a journal of the IMA. 2012 Mar;29(1):49–65.

18. Kathagen-Buhmann A, Schulte A, Weller J, Holz M, Herold-Mende C, Glass R, et al. Glycolysis and the pentose phosphate pathway are differentially associated with the dichotomous regulation of glioblastoma cell migration versus proliferation. Neuro-Oncology. 2016 Sep;18(9):1219–1229. Available from: https://www.ncbi.nlm.nih.gov/pmc/articles/PMC4998991/.

19. Dhruv HD, McDonough Winslow WS, Armstrong B, Tuncali S, Eschbacher J, Kislin K, et al. Reciprocal Activation of Transcription Factors Underlies the Dichotomy between Proliferation and Invasion of Glioma Cells. PLoS ONE. 2013 Aug;8(8):e72134. 00009. Available from: http://dx.doi.org/10.1371/journal.pone.0072134.

20. Vittadello ST, McCue SW, Gunasingh G, Haass NK, Simpson MJ. Examining Go-or-Grow Using Fluorescent Cell-Cycle Indicators and Cell-Cycle-Inhibiting Drugs. Biophysical Journal. 2020 Mar;118(6):1243–1247. Available from: http://www.sciencedirect.com/science/article/pii/S0006349520301119.

21. Wang CH, Matin S, George AB, Korolev KS. Pinned, locked, pushed, and pulled traveling waves in structured environments. Theoretical Population Biology. 2019;127:102–119.

22. Bayliss A, Volpert VA. Complex predator invasion waves in a Holling–Tanner model with nonlocal prey interaction. Physica D: Nonlinear Phenomena. 2017 May;346:37–58. Available from: http://www.sciencedirect.com/science/article/pii/S016727891630481X.

23. Wasserstein L. Markov processes over denumerable products of spaces describing large systems of automata. 1969 Jan;Available from: https://scinapse.io/papers/51701124.

24. Sanderson C, Curtin R. Armadillo: a template-based C++ library for linear algebra. Journal of Open Source Software. 2016 Jun;1(2):26. Available from: https://joss.theoj.org/papers/10.21105/joss.00026.

25. van der Meer D, Barthorpe S, Yang W, Lightfoot H, Hall C, Gilbert J, et al. Cell Model Passports—a hub for clinical, genetic and functional datasets of preclinical cancer models. Nucleic Acids Research. 2019 Jan;47(D1):D923–D929. Publisher: Oxford Academic. Available from: https://academic.oup.com/nar/article/47/D1/D923/5107576.

26. Barretina J, Caponigro G, Stransky N, Venkatesan K, Margolin AA, Kim S, et al. The Cancer Cell Line Encyclopedia enables predictive modelling of anticancer drug sensitivity. Nature. 2012 Mar;483(7391):603–607. 00591. Available from: http://www.nature.com/nature/journal/v483/n7391/full/nature11003.html.

27. Hafner M, Niepel M, Chung M, Sorger PK. Growth rate inhibition metrics correct for confounders in measuring sensitivity to cancer drugs. Nature Methods. 2016;13(6):521–527.

28. Hafner M, Heiser LM, Williams EH, Niepel M, Wang NJ, Korkola JE, et al. Quantification of sensitivity and resistance of breast cancer cell lines to anti-cancer drugs using GR metrics. Scientific Data. 2017 Nov;4. Available from: https://www.ncbi.nlm.nih.gov/pmc/articles/PMC5674849/.

29. Heiser LM, Sadanandam A, Kuo WL, Benz SC, Goldstein TC, Ng S, et al. Subtype and pathway specific responses to anticancer compounds in breast cancer. Proceedings of the National Academy of Sciences of the United States of America. 2012 Feb;109(8):2724–2729.

30. Daemen A, Griffith OL, Heiser LM, Wang NJ, Enache OM, Sanborn Z, et al. Modeling precision treatment of breast cancer. Genome Biology. 2013;14(10):R110.

31. Bräutigam K, Mitzlaff K, Uebel L, Köster F, Polack S, Pervan M, et al. Subtypes of Triple-negative Breast Cancer Cell Lines React Differently to Eribulin Mesylate. Anticancer Research. 2016 Jun;36(6):2759–2766.

32. Dai X, Cheng H, Bai Z, Li J. Breast Cancer Cell Line Classification and Its Relevance with Breast Tumor Subtyping. Journal of Cancer. 2017 Sep;8(16):3131–3141. Available from: https://www.ncbi.nlm.nih.gov/pmc/articles/PMC5665029/.

33. Hänzelmann S, Castelo R, Guinney J. GSVA: gene set variation analysis for microarray and RNA-Seq data. BMC Bioinformatics. 2013 Jan;14(1):7. Available from: https://doi.org/10.1186/1471-2105-14-7.

34. Croft D, Mundo AF, Haw R, Milacic M, Weiser J, Wu G, et al. The Reactome pathway knowledgebase. Nucleic Acids Research. 2014 Jan;42(Database issue):D472–D477. Available from: https://www.ncbi.nlm.nih.gov/pmc/articles/PMC3965010/.

35. Yang W, Soares J, Greninger P, Edelman EJ, Lightfoot H, Forbes S, et al. Genomics of Drug Sensitivity in Cancer (GDSC): a resource for therapeutic biomarker discovery in cancer cells. Nucleic Acids Research. 2013 Jan;41(Database issue):D955–D961. Available from: https://www.ncbi.nlm.nih.gov/pmc/articles/PMC3531057/.

36. Chen WYJ, Abatangelo G. Functions of hyaluronan in wound repair. Wound Repair and Regeneration. 1999;7(2):79–89. Available from: https://onlinelibrary.wiley.com/doi/abs/10.1046/j.1524-475X.1999.00079.x.

37. Ellis IR, Schor SL. Differential effects of TGF-beta1 on hyaluronan synthesis by fetal and adult skin fibroblasts: implications for cell migration and wound healing. Experimental Cell Research. 1996 Nov;228(2):326–333.

38. Fisher RA. THE WAVE OF ADVANCE OF ADVANTAGEOUS GENES. Annals of Eugenics. 1937 Jun;7(4):355–369. Available from: http://doi.wiley.com/10.1111/j.1469-1809.1937.tb02153.x.

39. Becht E, McInnes L, Healy J, Dutertre CA, Kwok IWH, Ng LG, et al. Dimensionality reduction for visualizing single-cell data using UMAP. Nature Biotechnology. 2018 Dec;.

40. Xu C, Su Z. Identification of cell types from single-cell transcriptomes using a novel clustering method. Bioinformatics (Oxford, England). 2015 Jun;31(12):1974–1980.

41. Sobol IM. Global Sensitivity Indices for Nonlinear Mathematical Models; 2004. .

42. Lim S, Nam H, Jeon JS. Chemotaxis Model for Breast Cancer Cells Based on Signal/Noise Ratio. Biophysical Journal. 2018;115(10):2034–2043.

43. Keller EF, Segel LA. Model for chemotaxis. Journal of Theoretical Biology. 1971 Feb;30(2):225–234. Available from: http://www.sciencedirect.com/science/article/pii/0022519371900506.

44. Anderson ARA, Rejniak KA, Gerlee P, Quaranta V. Microenvironment driven invasion: a multiscale multimodel investigation. Journal of mathematical biology. 2009 Apr;58(4-5):579–624. Available from: https://www.ncbi.nlm.nih.gov/pmc/articles/PMC5563464/.

45. Kimmel GJ, Gerlee P, Altrock PM. Time scales and wave formation in non-linear spatial public goods games. PLOS Computational Biology. 2019 Sep;15(9):e1007361. Publisher: Public Library of Science. Available from: https://journals.plos.org/ploscompbiol/article?id=10.1371/journal.pcbi.1007361.

46. Einstein A. On the Motion of Small Particles Suspended in Liquids at Rest Required by the Molecular-Kinetic Theory of Heat. 1905;17:208.

47. Andor N, Simonds EF, Czerwinski DK, Chen J, Grimes SM, Wood-Bouwens C, et al. Single-cell RNA-Seq of lymphoma cancers reveals malignant B cell types and co-expression of T cell immune checkpoints. Blood. 2018 Jan;p. blood–2018–08–862292. Available from: http://www.bloodjournal.org/content/early/2018/12/26/blood-2018-08-862292.

48. Birkbak NJ, Eklund AC, Li Q, McClelland SE, Endesfelder D, Tan P, et al. Paradoxical relationship between chromosomal instability and survival outcome in cancer. Cancer research. 2011 May;71(10):3447–3452. 00068 PMID: 21270108.

49. Morrissy AS, Garzia L, Shih DJH, Zuyderduyn S, Huang X, Skowron P, et al. Divergent clonal selection dominates medulloblastoma at recurrence. Nature. 2016 Jan;529(7586):351–357. 00000. Available from: http://www.nature.com/nature/journal/v529/n7586/full/nature16478.html.

50. Laughney AM, Elizalde S, Genovese G, Bakhoum SF. Dynamics of Tumor Heterogeneity Derived from Clonal Karyotypic Evolution. Cell Reports. 2015 Aug;12(5):809–820.

51. Elizalde S, Laughney AM, Bakhoum SF. A Markov chain for numerical chromosomal instability in clonally expanding populations. PLoS computational biology. 2018;14(9):e1006447.

52. Donovan P, Cato K, Legaie R, Jayalath R, Olsson G, Hall B, et al. Hyperdiploid tumor cells increase phenotypic heterogeneity within Glioblastoma tumors. Molecular bioSystems. 2014 Jan;.

53. Bailly M, Wyckoff J, Bouzahzah B, Hammerman R, Sylvestre V, Cammer M, et al. Epidermal Growth Factor Receptor Distribution during Chemotactic Responses. Molecular Biology of the Cell. 2000 Nov;11(11):3873–3883. Available from: https://www.ncbi.nlm.nih.gov/pmc/articles/PMC15043/.

54. Gulhati P, Bowen KA, Liu J, Stevens PD, Rychahou PG, Chen M, et al. mTORC1 and mTORC2 regulate EMT, motility, and metastasis of colorectal cancer via RhoA and Rac1 signaling pathways. Cancer Research. 2011 May;71(9):3246–3256.

55. James RG, Davidson KC, Bosch KA, Biechele TL, Robin NC, Taylor RJ, et al. WIKI4, a novel inhibitor of tankyrase and Wnt/ß-catenin signaling. PloS One. 2012;7(12):e50457.

56. Du L, Li X, Zhen L, Chen W, Mu L, Zhang Y, et al. Everolimus inhibits breast cancer cell growth through PI3K/AKT/mTOR signaling pathway. Molecular Medicine Reports. 2018 May;17(5):7163–7169.

57. Alalem M, Ray A, Ray BK. Metformin induces degradation of mTOR protein in breast cancer cells. Cancer Medicine. 2016 Oct;5(11):3194–3204. Available from: https://www.ncbi.nlm.nih.gov/pmc/articles/PMC5119975/.

58. Liu L, Li F, Cardelli JA, Martin KA, Blenis J, Huang S. Rapamycin inhibits cell motility by suppression of mTOR-mediated S6K1 and 4E-BP1 pathways. Oncogene. 2006 Nov;25(53):7029–7040.

59. Witelski TP, Ono K, Kaper TJ. ON AXISYMMETRIC TRAVELING WAVES AND RADIAL SOLUTIONS OF SEMILINEAR ELLIPTIC EQUATIONS. Natural Resource Modeling. 2008 Jun;13(3):339–388. Available from: http://doi.wiley.com/10.1111/j.1939-7445.2000.tb00039.x.

60. Lin CH, Lee JK, LaBarge MA. Fabrication and use of microenvironment microarrays (MEArrays). Journal of Visualized Experiments: JoVE. 2012 Oct;(68).